



**Defect-rich and ultrathin N doped carbon nanosheets as  
advanced trifunctional metal-free electrocatalysts for ORR,  
OER and HER**

Journal:	<i>Energy &amp; Environmental Science</i>
Manuscript ID	EE-ART-11-2018-003276.R1
Article Type:	Paper
Date Submitted by the Author:	20-Nov-2018
Complete List of Authors:	<p>Jiang, Hao; Central South University, Gu, Jinxing; Nanjing Normal University, School of Chemistry and Materials Science Zheng, Xusheng ; University of Science and Technology of China Liu, Min; Central South University, Department of Physics Qiu, Xiaoqing; Central South University College of Chemistry and Chemical Engineering, Wang, Liangbing; Central South University, School of Materials Science and Engineering Li, Wenzhang; Central South University, College of Chemistry and Chemical Engineering Chen, Zhongfang; University of Puerto Rico, Department of Chemistry Ji, Xiaobo; Central South University, College of Chemistry and Chemical Engineering Changsha, Hunan, China, ; Li, Jie; Central South University, College of Chemistry and Chemical Engineering</p>



Journal Name

ARTICLE

## Defect-rich and ultrathin N doped carbon nanosheets as advanced trifunctional metal-free electrocatalysts for ORR, OER and HER

Hao Jiang,<sup>ab</sup> Jingxing Gu,<sup>c</sup> Xusheng Zheng,<sup>d</sup> Min Liu,<sup>e</sup> Xiaoqing Qiu,<sup>a</sup> Liangbing Wang,<sup>f</sup> Wenzhang Li,<sup>\*ag</sup> Zhongfang Chen,<sup>\*c</sup> Xiaobo Ji,<sup>a</sup> Jie Li,<sup>\*ag</sup>

Received 00th January 20xx,  
Accepted 00th January 20xx

DOI: 10.1039/x0xx00000x

[www.rsc.org/](http://www.rsc.org/)

Rational design and facile preparation of non-noble trifunctional electrocatalysts with high performance, low cost and strong durability for oxygen reduction reaction (ORR), oxygen evolution reaction (OER) and hydrogen evolution reaction (HER) is highly demanded, but remains as a big challenge. Herein, we report a spontaneous gas-foaming method to prepare nitrogen doped ultrathin carbon nanosheets (NCNs) by simply pyrolysing the mixture of citric acid and  $\text{NH}_4\text{Cl}$ . Under the optimized pyrolysis temperature (carbonized at 1000 °C) and mass ratio of precursors (1:1), the synthesized NCN-1000-5 sample possesses ultrathin sheet structure, ultrahigh specific surface area ( $1793 \text{ m}^2 \text{ g}^{-1}$ ), and rich edge defects, and exhibits low overpotential and robust stability for ORR, OER and HER. By means of density functional theory (DFT) computations, we revealed that the intrinsic active sites for ORR, OER and HER are the carbon atoms located at the armchair edge and adjacent to the graphitic N dopants. When practically worked as a catalyst in rechargeable Zn-air batteries, a high energy density ( $806 \text{ Wh kg}^{-1}$ ), a low charge/discharge voltage gap (0.77 V) and an ultralong cycling life (over 330 h) were obtained at  $10 \text{ mA cm}^{-2}$  for NCN-1000-5. This work not only presents a versatile strategy to develop advanced carbon materials with ultrahigh specific surface area and abundant edge defects, but also provides useful guidance for designing and developing multifunctional metal-free catalyst for various energy-related electrocatalytic reactions.

### Introduction

High energy consumption, serious pollution and non-renewable fossil fuels are not in conformity with the requirements of sustainable development of human society. Clean, high capacity and renewable energy storage and conversion techniques such as fuel cells, metal-air batteries and water splitting system, are promising alternatives for the traditional fossil fuels.<sup>1-4</sup> Electrochemical oxygen reduction reaction (ORR), oxygen evolution reaction (OER), and hydrogen evolution reaction (HER) are at the heart of the above

mentioned renewable energy technologies. However, efficient catalysts are desired to overcome the sluggish kinetics and large overpotential of these electrochemical reactions. To date, Pt-based noble metal remains the most efficient electrocatalyst for ORR and HER, whereas  $\text{IrO}_2$  and  $\text{RuO}_2$  are highly active towards OER.<sup>5-8</sup> Nevertheless, the scarcity, high cost and poor tolerance of these platinum group metals (PGMs) severely hinder their large-scale applications. Therefore, developing low cost, highly active and robust catalysts based on earth-abundant non-noble metals for these important electrocatalytic processes is paramount and highly rewarding.

To date, tremendous efforts have been given in developing advanced non-noble metals catalysts (NNMCs) to substitute Pt and Ru-based catalysts,<sup>3, 9, 10</sup> among which heteroatom (N, P, S, or B) doped carbon materials distinguish themselves as one of the most promising substitutes of NNMCs for either ORR, OER or HER due to their low cost, high activities and robust stability.<sup>11</sup> For example, we have recently demonstrated that dual atoms (N and P) co-functionalized porous carbon networks possess superior ORR activity over a broad pH range of aqueous media.<sup>12</sup> Qiao's group prepared a self-supported N-doped carbon hydrogel film, which is greatly favorable for OER.<sup>13</sup> As for HER, N and P-doped graphite carbon coupled with carbon cloth showed a low HER overpotential of 240 mV at  $10 \text{ mA cm}^{-2}$ .<sup>14</sup> Moreover, Dai and

<sup>a</sup> School of Chemistry and Chemical Engineering, Central South University, Changsha, 410083, China. E-mail: liwenzhang@csu.edu.cn; lijieliu@csu.edu.cn. Tel./fax: +86-731-88879616

<sup>b</sup> College of Materials and Chemical Engineering, Hunan City University, Yiyang, 413000, China.

<sup>c</sup> Department of Chemistry, University of Puerto Rico Rio Piedras Campus, San Juan, PR 00931, USA. E-mail: zhongfangchen@gmail.com

<sup>d</sup> Hefei National Laboratory for Physical Sciences at the Microscale, National Synchrotron Radiation Laboratory, University of Science and Technology of China, Hefei, Anhui, 230026, China.

<sup>e</sup> Institute of Super-microstructure and Ultrafast Process in Advanced Materials, School of Physics and Electronics, Central South University, Changsha, Hunan, China.

<sup>f</sup> School of materials science and engineering, Central South University, Changsha, Hunan, China.

<sup>g</sup> Hunan Provincial Key Laboratory of Chemical Power Sources, Central South University, Changsha 410083, Hunan, China.

† Electronic Supplementary Information (ESI) available. See DOI: 10.1039/x0xx00000x

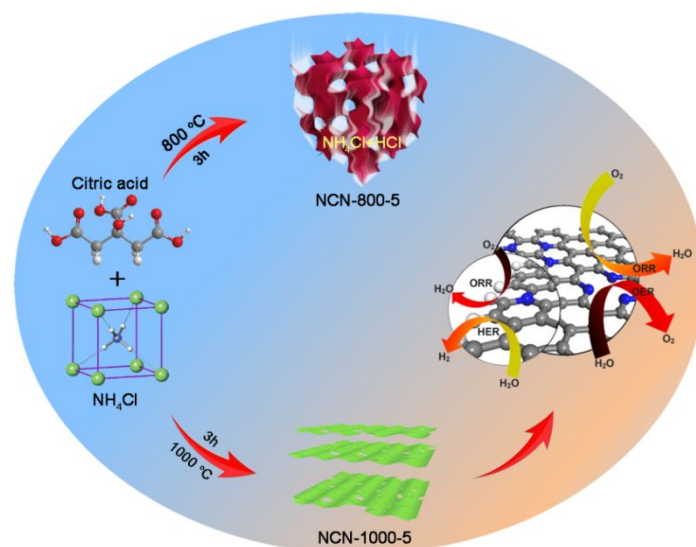
coworkers developed a series of doped nanocarbon materials, including N-doped porous carbon nanofiber films, N and P co-doped mesoporous carbon foam and porous carbon networks, which have novel structures, high specific surface area, and more importantly, outstanding bifunctional activity toward ORR/OER or ORR/HER.<sup>1, 15-17</sup> Although so many doped carbon materials show remarkable electrocatalytic activity in a separate ORR, or OER, or HER, they can scarcely function well concurrently toward OER, HER and ORR due to their unstable or inactive nature in an unfavorable pH environment. Until recently, Hu et al. prepared N, S co-doped graphitic sheets (SHG) with a unique hierarchical structure and exhibited remarkable trifunctional electrocatalytic activity for ORR, OER and HER.<sup>18</sup> However, the synthesis of SHG suffers from removing template with aqua-regia and multi-step pyrolysis process, which has the shortcomings of multistep, time-consuming and high cost. Therefore, exploring facile and universal methods to fabricate carbon materials with unique structure, high specific surface area and multifunctional electrocatalytic feature is highly desired, but remains a challenge. Furthermore, the research on the catalytic mechanisms and activity sites of heteroatom doped carbon materials toward OER, HER and ORR is also insufficient. To the best of our knowledge, experimental and theoretical research of N doped carbon materials concurrently toward ORR, OER and HER has never been reported.

In this work, we put forward a spontaneous gas-foaming strategy to synthesize N doped ultrathin carbon nanosheets (NCNs) through a simple one-step carbonization of citric acid and  $\text{NH}_4\text{Cl}$ . This method introduces rich defects and large quantity of micropores into the NCNs. Especially, the sample (NCN-1000-5) obtained at 1000 °C with a mass ratio of 1:1 possesses ultrathin sheet structure (the edge thickness only 4 graphitic layers), ultrahigh specific surface area, rich edge defects and extraordinary trifunctional activity. It shows

superior ORR activity (onset potential) even better than commercial Pt/C and comparable OER activity to  $\text{IrO}_2$  in alkaline electrolytes. Moreover, it is also highly active and stable towards HER in acidic media. Our DFT computations revealed that graphitic N dopants and the abundant carbon edge defects in the porous structure are responsible for the trifunctional electrocatalytic activity of NCN-1000-5. As a showcase for its application in energy devices, we assembled a conventional Zn-air battery with NCN-1000-5 as air cathode catalyst, which exhibits outstanding rechargeable performance and ultrastrong durability.

## Results and discussion

The NCNs were prepared by a spontaneous gas-foaming approach using citric acid and  $\text{NH}_4\text{Cl}$  as raw materials (Scheme 1). Due to its abundant carbon atoms and powerful combining capacity to form complexes, citric acid was selected as carbon source to prepare NCNs. As for  $\text{NH}_4\text{Cl}$ , it not only served as a nitrogen source for NCNs, but also acted as foaming agent to construct the cross-linked 3D porous networks structure, since  $\text{NH}_4\text{Cl}$  can be decomposed into  $\text{NH}_3$  and  $\text{HCl}$  during the carbonization process. On one hand, the resulting  $\text{NH}_3$  can further combine with the carboxyl from citric acid through a dehydration-condensation reaction, which *in-situ* introduces the N atoms uniformly into graphite lattice after carbonization; on the other hand, the large amounts of released  $\text{NH}_3$  and instantaneous high internal pressure can blow the carbon matrix to form defect-rich and ultrathin carbon nanosheets (Figure S1). The optical images of the preparation process for NCNs are presented in Figure S2. Besides, it needs to be emphasized that the spontaneous gas-foaming strategy is versatile and highly valuable for preparing advanced carbon materials with ultrahigh specific surface area and abundant porous structures (Figure S3).



**Scheme 1** The schematic procedure for synthesizing the NCNs.

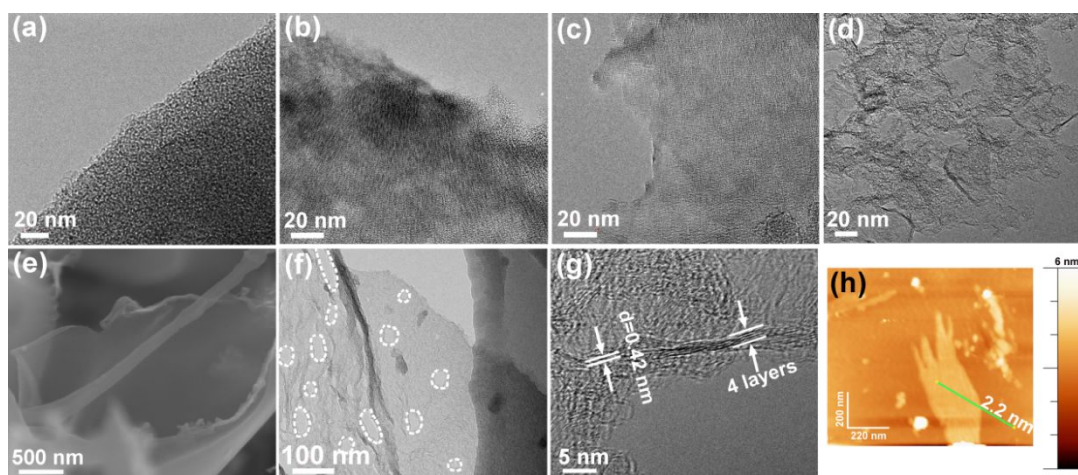


**Figure 1** TEM images of (a) C-1000, (b) NCN-800-5, (c) NCN-900-5 and (d) NCN-1000-5; (e) SEM, (f) TEM, (g) HRTEM and (h) AFM images of NCN-1000-5.

To investigate the evolution process of NCNs, a series of conditional experiments on carbonization temperature and the mass ratio of precursors are implemented. Figure S4 and Figure S5 present the scanning electronic microscopy (SEM) and transmission electron microscopy (TEM) images of the obtained products carbonized at different temperature. Without the presence of  $\text{NH}_4\text{Cl}$ , only large carbon blocks (C-1000) can be obtained even carbonized at 1000 °C (Figure 1a and S4a). After carbonizing the precursors (the mass ratio is 1:1) at a relatively low temperature of 800 °C, the rudiment of thick carbon nanosheets (NCN-800-5) with porous architecture emerged (Figure 1b and S4b). When the carbonization temperature rapidly rises to 1000 °C, cross-linked 3D porous carbon networks (NCN-1000-5) can be clearly observed, which is composed of interconnected ultrathin carbon nanosheets with a thickness of  $\sim 2$  nm (Figure 1e and 1h). The corresponding TEM images (Figure 1d and 1f) further reveal that the existence of numerous mesoporous and nanoporous on the graphene-like ultrathin carbon nanosheets. High-resolution TEM (HRTEM) image shows that the edges of NCN-1000-5 are only 4 graphitic layers (Figure 1g). A lattice spacing of 0.42 nm and distinct diffraction rings can be observed from the high-resolution TEM (HRTEM) image (Figure 1c) and selected-area electron diffraction (SAED) pattern (Figure S6) of NCN-1000-5, which are corresponding to the (002) plane of typical hexagonal pattern for graphitic carbon.<sup>12, 19</sup> The elemental mapping images of NCN-1000-5 (Figure S7) indicate the evenly distribution of C, O and N elements in this sample. Atomic force microscope (AFM) images clearly demonstrate that the thickness of NCNs gradually decreases from 800 to 1000 °C (Figure S8). Thus, the carbonization temperature is crucial for regulating the porosity and thickness of carbon nanosheets. Moreover, the mass ratio of citric acid to  $\text{NH}_4\text{Cl}$  also plays a significant role in influencing the morphology and structure of the NCNs (Figure S9).

We employed X-ray diffraction (XRD) pattern and Raman spectra to examine the crystal texture of the pyrolytic carbon products. The two broad diffraction peaks at  $2\theta \approx 24.8$  and  $44^\circ$  in XRD (Figure S10a) are well indexed to the (002) and (101) facets of graphite.<sup>20, 21</sup> The corresponding Raman spectra clearly show characteristic D and G bands at  $1340\text{ cm}^{-1}$  and  $1591\text{ cm}^{-1}$ , which are assigned to disordered carbon atoms and  $\text{sp}^2$  hybridized graphitic carbon atoms, respectively (Figure S10b).<sup>22, 23</sup> The gradually increased values of  $I_D/I_G$  for NCNs, which imply the insertion of N atoms under high pyrolytic temperature, indicate the formation of more edges and topological defects in NCNs.<sup>12, 24</sup> These abundant defect sites can modulate and tune the electronic and surface properties of NCN-1000-5, and thus optimize the adsorption energies of electrochemical catalysis steps.<sup>24, 25</sup>

The surface area and porous structure of the resultant samples were further characterized by  $\text{N}_2$  adsorption/desorption measurements. The type I isotherm curves and rapid nitrogen uptake ( $P/P_0 < 0.1$ ) (Figure 2c) confirm the existence of numerous micropores and mesopores in NCNs.<sup>26, 27</sup> The specific surface area of NCNs increases remarkably with increasing the carbonization temperature and the mass of  $\text{NH}_4\text{Cl}$  (Table S1). Particularly, NCN-1000-5 has the highest ultrahigh specific surface area of  $1793\text{ cm}^2\text{ g}^{-1}$  among all the synthesized NCNs samples (nearly 48 times larger than that of C-1000,  $37\text{ cm}^2\text{ g}^{-1}$ ), and this value outperforms the vast majority of doped carbon materials, *e.g.* N, P -doped mesoporous nanocarbon foams ( $1663\text{ cm}^2\text{ g}^{-1}$ ),<sup>1</sup> P, S -codoped carbon nitride sponges ( $1474\text{ cm}^2\text{ g}^{-1}$ ),<sup>28</sup> N, S-enriched porous carbon ( $830\text{ cm}^2\text{ g}^{-1}$ ),<sup>29</sup> N, P-doped porous carbon networks ( $743\text{ cm}^2\text{ g}^{-1}$ )<sup>12</sup> and N, S -doped graphitic sheets ( $576\text{ cm}^2\text{ g}^{-1}$ ).<sup>18</sup> The corresponding pore size distribution curves indicate that the NCNs possess large pore volume and are dominated by micropores and mesopores (Figure 2d and Table S1). The existence of microporous greatly enhances the specific surface

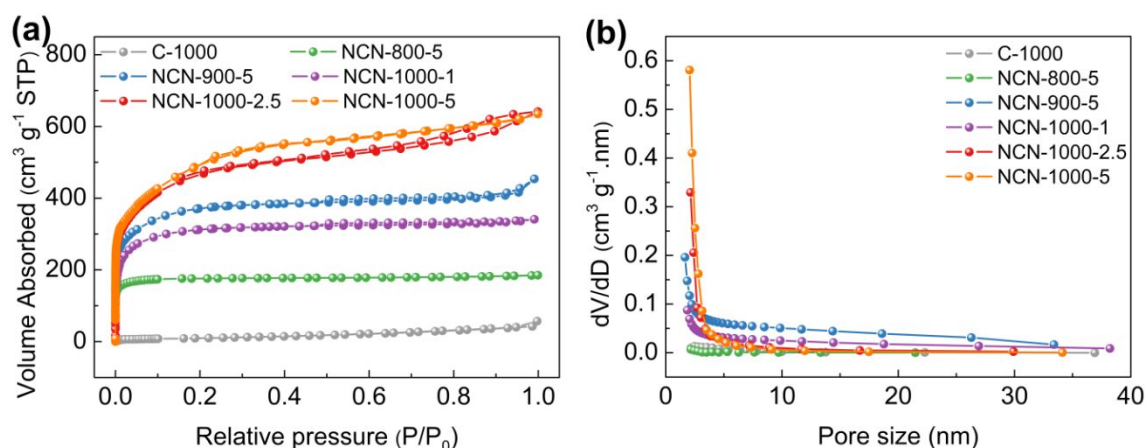


**Figure 2** (a)  $N_2$  adsorption/desorption isotherms and (b) pore size distribution of C-1000, NCN-800-5, NCN-900-5, NCN-1000-1, NCN-1000-2.5 and NCN-1000-5.

areas of NCNs and provides a high density of active sites, while the mesopores are conducive to creating more structural defects and transporting the reaction mediates. The ultrahigh specific surface area and large pore volume of NCN-1000-5 are expected to facilitate the mass transport and expose more active surface sites for electrochemical reactions.<sup>12, 30, 31</sup>

X-ray photoelectron spectroscopy (XPS) was executed to investigate the chemical composition and bonding configurations of the NCNs. Figure 3a and Figure S10 confirm the presence of C, O and N elements in NCNs, which are in accordance with the elemental mapping results (Figure S7). The corresponding atomic percentages of the above elements are listed in Table S2. The fitted high-resolution C 1s spectrum can be classified into four peaks at about 284.8, 285.7, 286.2 and 288.3 eV, corresponding to C-C, C-N, C-O and C=O, respectively (Figure 3b).<sup>18, 32</sup> The successful doping of N atoms into carbon skeleton is verified by the corresponding high-resolution N 1s spectrum. As displayed in Figure 3d and Figure S11, the N 1s of NCNs can be classified into pyridinic N (398.3 eV), pyrrolic N (399.8 eV), graphitic N (401.1 eV) and pyridinic N oxide (402-406 eV), respectively.<sup>33, 34</sup> It has been generally accepted that pyridinic N, pyrrolic N and graphitic N play significant roles in the reversible oxygen reduction/evolution reactions and HER processes.<sup>18, 35</sup> Further investigations reveal that the percentage of pyridinic N and pyrrolic N remarkably decreased, whereas the content of graphitic N increases from 800 to 1000 °C (Figure 3c and Table S3). This is because pyridinic N and pyrrolic N are thermolabile and incline to transform into graphitic N with increasing temperature. Elemental analysis of the possible existence of transition metals in NCNs catalysts was further conducted using inductively coupled plasma-atomic emission spectroscopy (ICP-AES). The detected total transition metal (Fe, Co and Ni) content of NCN-1000-5 is below 0.01 wt% (Table S4), indicating that the amount of metal Fe, Co and Ni is negligible. In addition, the functional groups on the surface of NCNs were

further identified by Fourier transform infrared spectra (FT-IR), as displayed in Figure S12.

To further investigate the electronic structure and local chemical configuration of the carbon-based catalysts, the near edge X-ray absorption fine structure (NEXAFS) experiments were carried out. The obtained C K-edge spectra of C-1000 and NCNs are extremely similar (Figure 4a), indicating similar environments of carbon skeletons present. Defects at 284.0 eV are assigned to the low-coordinated carbon atoms at the edges of NCNs, which can lead to the rehybridization of C atoms and break the integrity of  $\pi$  conjugation.<sup>36-38</sup> In addition, a portion of active unpaired  $\pi$  electron locates at each edge carbon atom, which can effectively facilitate electron transfer to  $O_2$ .<sup>39</sup> The excitations of  $\pi^*$  at 285.4 eV (peak C1) and  $\sigma^*$  at 291~293 eV (peak C3) are attributed to C=C and C-C species in C-1000 and NCNs, respectively. The peak C2 at 288.4 eV suggests the formation of C-N-C or C-O-C.<sup>40, 41</sup> Due to the decomposition of oxygen-containing functional groups and the loss of N atoms at high pyrolysis temperature, the intensity of peak C2 from NCN-800-5 to NCN-1000-5 displays a decrease. In contrast to the overlapping peaks of XPS analysis (Figure 3d), three well-defined peaks below the ionisation potential of N corresponding to transitions from 1s into the  $\pi^*$  orbitals and a broad peak from energies 407~408 eV corresponding to the  $\sigma^*$  resonance can be observed in N K-edge NEXAFS spectra (Figure 4b). Among them, the resonances of  $\pi^*$  at 398.1 (N1), 399.2 (N2) and 401.4 eV (N3) are contributed from pyridinic N, pyrrolic N and graphitic N, respectively.<sup>42</sup> The excitations of  $\sigma^*$  at 407~408 eV is attributed to C-N-C or C-N.<sup>41</sup> The existence of N species improve the charge mobility of carbon matrix by introducing electron-donor characteristics and enhancing the carbon catalytic activity in electron-transfer reactions.<sup>43</sup>

#### Catalytic activity towards ORR

The catalytic activity of NCNs toward ORR was initially investigated in 0.1 M KOH electrolyte. The most positive

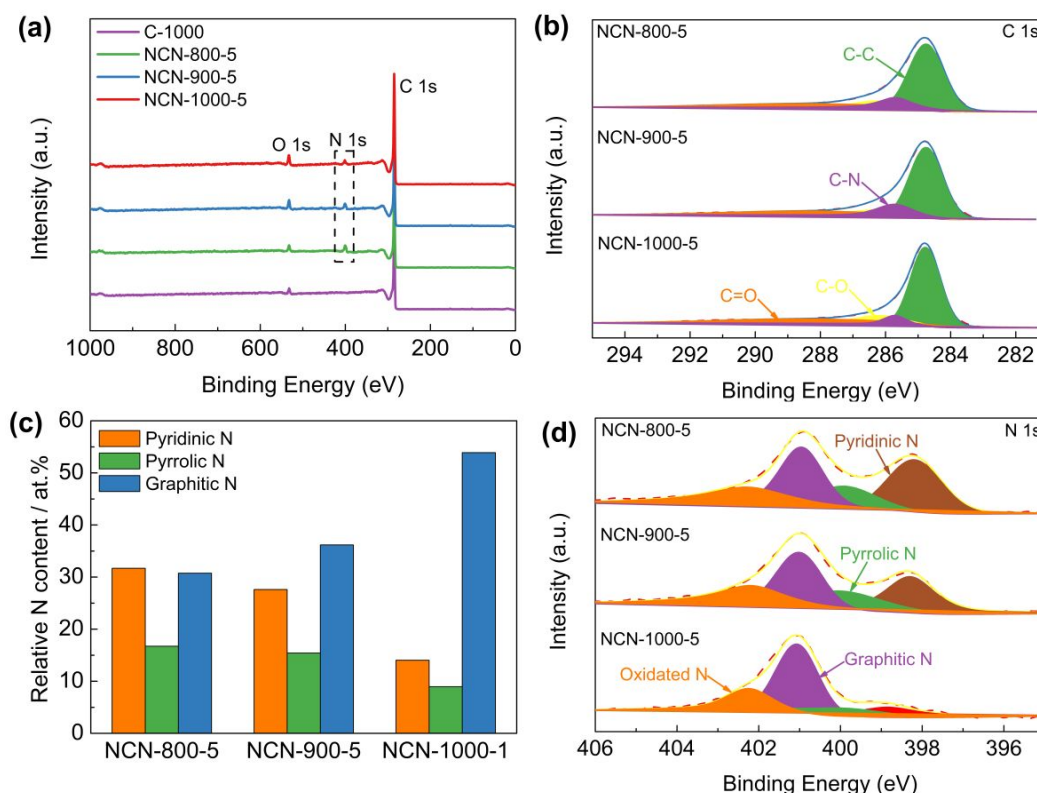


**Figure 3** (a) The wide XPS survey spectra of C-1000, NCN-800-5, NCN-900-5 and NCN-1000-5; (b) High resolution C 1s spectra, (c) the contents of different nitrogen kinds and (d) N 1s spectra of NCN-800-5, NCN-900-5 and NCN-1000-5.

reduction peak potential ( $E_p$ ) at 0.86 V was observed in the cyclic voltammetry (CV) curves (Figure 5a and Figure S13a), implying that NCN-1000-5 possesses superior ORR activity. The linear scan voltammogram (LSV) curves (Figure 5b and Figure S13b) further confirm the excellent ORR performance of NCN-1000-5, with a positive onset potential ( $E_{onset}$ ) of 0.95 V, a half-wave potential ( $E_{1/2}$ ) of 0.82 V, and a high limiting current density of 6.13 mA cm<sup>-2</sup> (Table S5). Remarkably, these performance indexes of NCN-1000-5 are comparable to those

of Pt/C (Table S4) and some advanced metal free ORR catalysts reported in literature (Table S6). The comparable Tafel slopes for NCN-1000-5 (86 mV dec<sup>-1</sup>) and Pt/C (84 mV dec<sup>-1</sup>) signify the transfer of the first electron may be the rate-determining step in ORR catalyzed by them (Figure 4c).<sup>44-46</sup> The linear and paralleled Koutecky-Levich (K-L) plots (Figure S15) derived from LSV curves (Figure S14) reflect a first-order reaction with respect to the dissolved O<sub>2</sub>.<sup>47</sup> The calculated electron transferred number ( $n$ ) for NCN-1000-5, 3.92 at 0.5 V based on

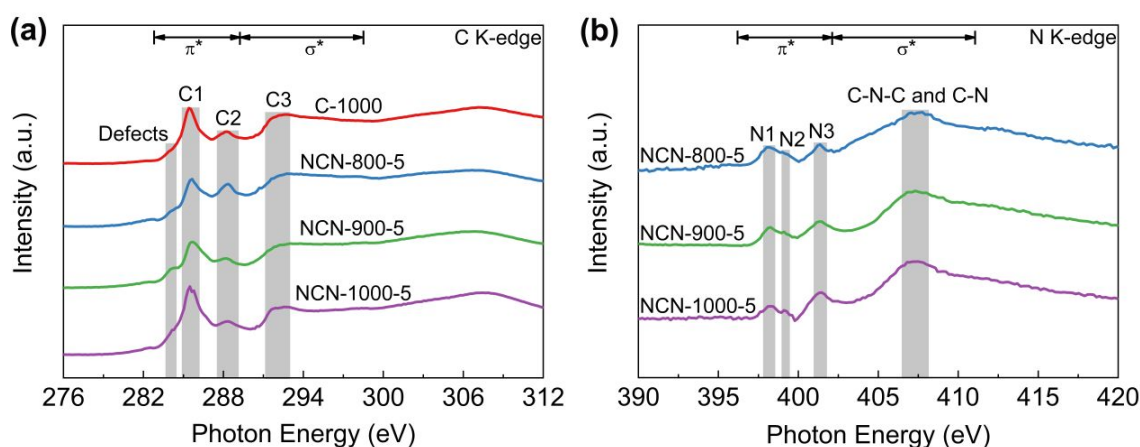


**Figure 4.** (a) C K-edge and (b) N K-edge NEXAFS spectra of C-1000, NCN-800-5, NCN-900-5 and NCN-1000-5.

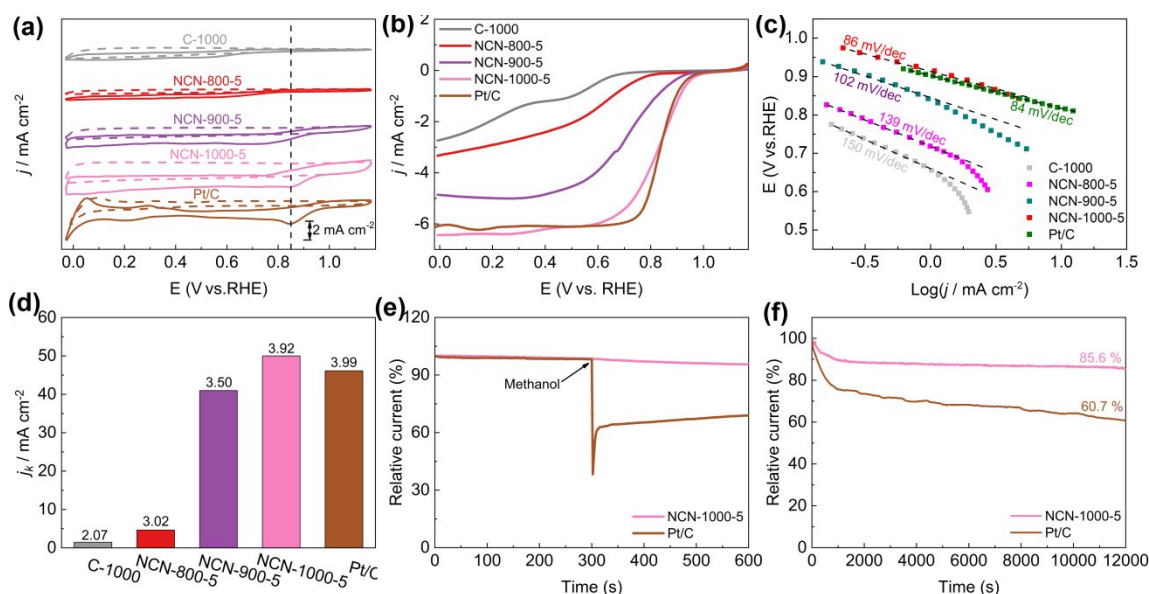


**Figure 5** (a) CV curves of C-1000, NCN-800-5, NCN-900-5, NCN-1000-5 and Pt/C in  $N_2$  (dotted line) and  $O_2$  (solid line)-saturated 0.1 M KOH ( $50 \text{ mV s}^{-1}$ ); (b) LSV curves and (c) Tafel plots of various catalysts (1600 rpm,  $5 \text{ mV s}^{-1}$ ); (d) electrochemical activity given as the kinetic current density ( $J_k$ ) at 0.5 V (vs. RHE) for various catalysts, the numeral on the bar represents the corresponding electron transfer number; (e) methanol crossover tolerance and (f) durability tests of NCN-1000-5 and Pt/C at 0.67 V (1600 rpm).

K-L plots, confirms an apparent  $4e^-$  pathway to reduce  $O_2$ . The corresponding kinetic current density ( $J_k$ ) of NCN-1000-5 is  $50 \text{ mA cm}^{-2}$  at this potential (Figure 4d), which is even slightly larger than that of Pt/C ( $46.3 \text{ mA cm}^{-2}$ ).

Besides the high ORR activity, the NCN-1000-5 also exhibits super immunity to methanol crossover (Figure 5e). The ORR relative current of Pt/C shows a cliff-like drop after 0.5 mL methanol (3 M) is added into electrolyte at 300 s, whereas the current of NCN-1000-5 keeps almost unchanged. Furthermore, a high current retention (85.6 %) after 12000 s continuous test demonstrated the long-term stability of NCN-1000-5 (Figure 5f). These results clearly demonstrate that the NCN-1000-5 possesses excellent activity, strong stability and high selectivity toward ORR in alkaline media, all of which are extremely significant for practical applications. XPS results reveal that the oxygen content of NCN-1000-5 increases after long-term  $i-t$  test (Figure S16 and Table S7). It is possible that the nitrogen-doped sample has been partly oxidized by oxygen atoms and some oxygen containing functional groups were formed on the N doped carbon nanosheets.

More surprisingly, the NCN-1000-5 sample also displayed preeminent ORR activity and stability in acidic media, as depicted in Figure S17. Similar to the situation described in alkaline media, the NCN-1000-5 undergoes first-order reaction kinetics and exhibits an apparent  $4e^-$  pathway to reduce  $O_2$  in acidic media, as indicated by the LSV curves (Figure S18) and linear K-L plots (Figure S19). The  $E_{\text{onset}}$  of NCN-1000-5 is 0.78 V, only 20 mV more negative than that of Pt/C in 0.5 M  $H_2SO_4$  electrolyte (Table S8). The slightly less activity in acidic media

may be due to the protonation of N atoms and the subsequent adsorption of  $SO_4^{2-}$  anion on the surface of NCN-1000-5, which covers up some active sites.<sup>48</sup> Although the ORR activity of NCN-1000-5 is slightly worse than that of Pt/C in acidic media, it still outperforms some metal-free catalysts reported in literatures (Table S9).

### Catalytic activity towards OER

To demonstrate the trifunctional activity, we then evaluated the OER performance of NCNs. Similar to the case for ORR, the NCN-1000-5 exhibits much better OER activity than that of other NCNs samples and pristine carbon blocks (C-1000). The  $E_{\text{onset}}$  and measured potential at a current density of  $10 \text{ mA cm}^{-2}$  ( $E_{j=10}$ ) of NCN-1000-5 (Figure 6a and 6b) are 1.55 and 1.64 V, respectively, which are lightly inferior to those of  $IrO_2$  (1.48 V and 1.59 V) but comparable to many advanced NNMCs for OER (Table S10). A small current was detected in the LSV curves of NCNs before the OER occurred (Figure 6a), which may be caused by the side reactions of some oxygenic functional groups.<sup>13</sup> The enhanced OER kinetics of NCN-1000-5 was further testified by its small Tafel slope of  $142 \text{ mV dec}^{-1}$  at low overpotential (Figure 6c). The NCN-1000-5 also keeps high stability with a consistent OER current after 12000 s continuous operations (Figure 6d). The strong durability of NCN-1000-5 is reconfirmed by its LSV curves with little variation after 500 cycles (the insert in Figure 6d). Moreover, NCN-1000-5 shows the smallest Nyquist circle in the electrochemical impedance spectroscopy (EIS) compared with other NCNs samples (Figure S20), demonstrating its quickest

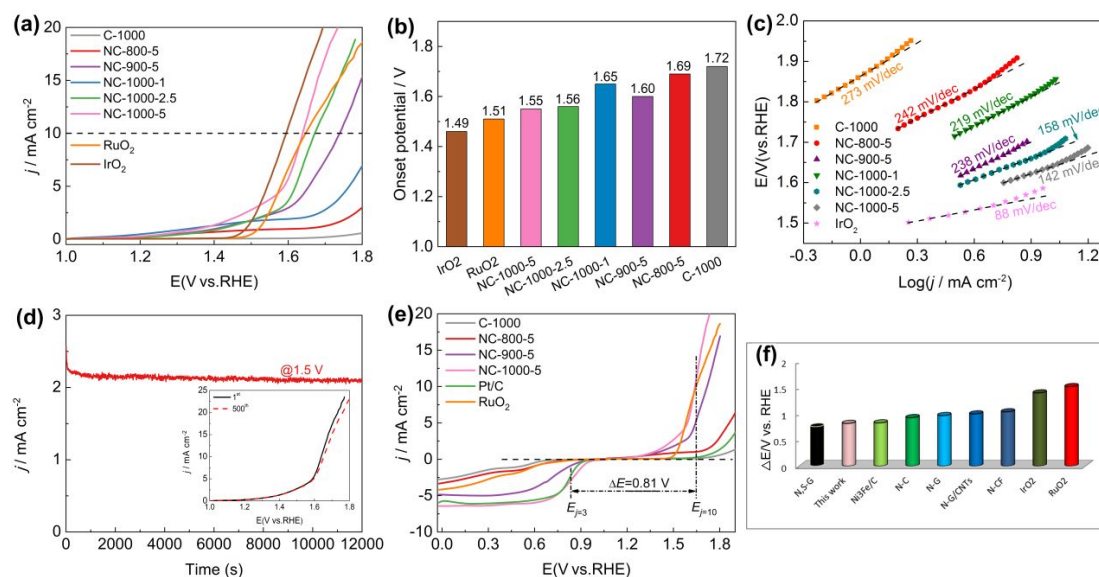


**Figure 6** (a) LSV curves of C-1000, NCN-800-5, NCN-900-5, NCN-1000-1, NCN-1000-2.5, NCN-1000-5, RuO<sub>2</sub> and IrO<sub>2</sub> in O<sub>2</sub>-saturated 0.1 M KOH electrolyte (1600 rpm, 5 mV s<sup>-1</sup>); (b) onset potentials and (c) Tafel plots of various catalysts; (d) the *i-t* plot at the applied potential of 1.5 V (vs. RHE), inset shows the LSV curves of NCN-1000-5 before and after 500 CV cycles; (e) the overall LSV curves for ORR and OER of various catalysts at 1600 rpm; (f) comparison of  $\Delta E$  for NCN-1000-5 and various carbon-based materials.

charge transfer ability.<sup>49</sup> The potential difference ( $\Delta E$ , defined in equation S4) of OER and ORR is generally used to estimate the performance of bifunctional oxygen electrode catalyst.<sup>50, 51</sup> A better bifunctional catalyst tends to have a smaller value of  $\Delta E$ . Remarkably, the NCN-1000-5 shows a low  $\Delta E$  value of 0.81 V (Figure 6e), which is smaller than that of RuO<sub>2</sub> (1.51 V) and some reported bifunctional electrocatalysts (Figure 6f and Table S11).

#### Catalytic activity towards HER

Furthermore, we observed the exciting HER activity of NCNs in N<sub>2</sub>-saturated 0.5 M H<sub>2</sub>SO<sub>4</sub> electrolyte. As displayed in Figure 7a and Figure S21a, the NCNs samples exhibits greatly improved HER activity as compared with the pristine carbon blocks (C-1000) and glass carbon (GC). Remarkably, the NCN-1000-5 shows a superior HER performance with almost the same positive  $E_{\text{onset}}$  to Pt/C (-0.03 V), which is much positive than that of other as-prepared NCNs samples in this work. At a current density of 10 mA cm<sup>-2</sup> ( $E_{j=10}$ ), the obtained potential for NCN-1000-5 (-0.09 V) is only 51 mV more negative than that of Pt/C (Figure 7b). The excellent kinetic property of NCN-1000-5 is confirmed by its small Tafel slope of 43 mV dec<sup>-1</sup> (Figure 7d and Figure S21b).<sup>52</sup> In fact, the HER performance of NCN-1000-5 is also better than that of many reported carbon materials, as presented in Figure 7c and Table S12. Figure 6e displays the similar LSV curves at sweep speeds from 5 to 100 mV s<sup>-1</sup> for NCN-1000-5, suggesting its robust stability for highly active electrochemical process. The excellent stability of NCN-1000-5 was further verified by its almost unchanged LSV curves after

500 CV cycles (Figure 7f) and a consistent HER current after 12000 s continuous operation at -0.15 V (the insert in Figure 7f).

#### Catalytic mechanisms revealed by DFT computations

Our experimental studies strongly demonstrate that the hierarchical porous and defect-rich NCN-1000-5 is a promising cost-effective and trifunctional electrocatalyst for ORR, OER and HER simultaneously. Then, we performed systematic DFT computations to reveal the underlying catalytic mechanisms and the active sites of NCNs for ORR, OER and HER.

To examine the effect of doping type (graphitic, pyridinic or pyrrolic N), doping concentration, and the distance of active site away from the hole edges, we constructed two types of structural models (totally 14 models) in our theoretical studies. The first is the graphene monolayer doped by N atoms, which serves as a model to study the active sites far away from the hole edges; the second is the graphene nanoribbons doped by N atoms, which is used to simulate the active sites on or close to the hole edges. The models are sketched in Figure 8, and the 14 different models are detailed in Supporting Information. The possible active sites for ORR and OER on N-doped graphene are basically the carbon atoms adjacent to the N dopant.<sup>53-55</sup> These carbon atoms have either high positive atomic charge or high spin density, and are labelled as M-x, where M is the model, and x refers to the numbering of the active site where reaction occurs. For instance, the site 2 of the one-graphitic-N doped armchair nanoribbon (A) is termed as A-2.

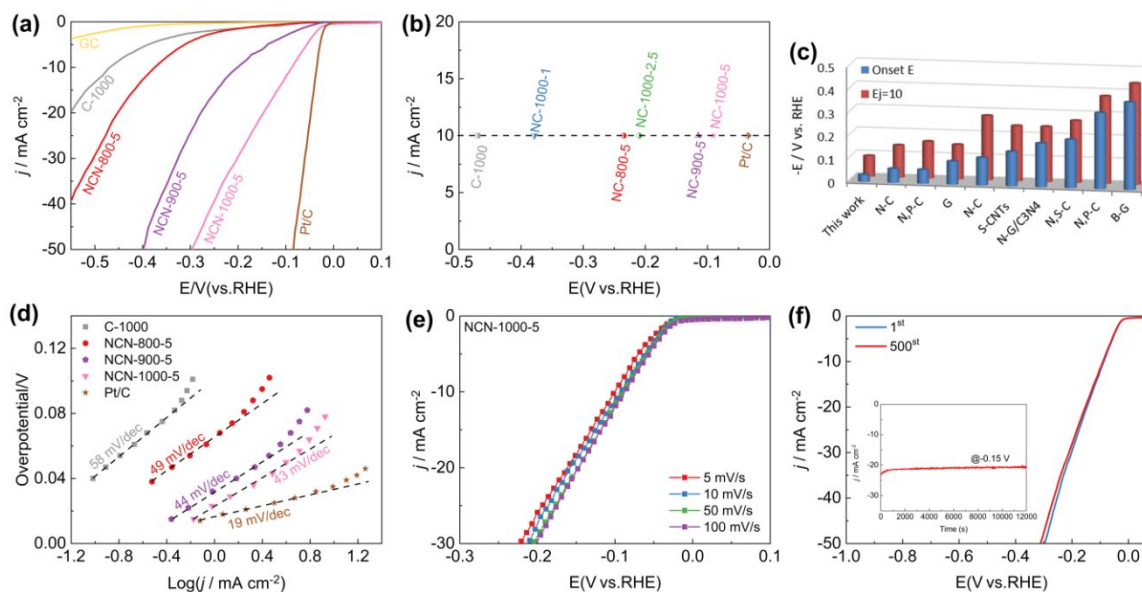


**Figure 7** (a) LSV curves of GC, C-1000, NCN-800-5, NCN-900-5, NCN-1000-5 and Pt/C in  $N_2$ -saturated 0.5 M  $H_2SO_4$  ( $5\text{ mV s}^{-1}$ ); (b) the measured potential at a current density of  $10\text{ mA cm}^{-2}$  ( $E_{j=10}$ ) for various catalysts; (c) comparison of the activities ( $E_{\text{onset}}$  and  $E_{j=10}$ ) for NCN-1000-5 and various carbon-based materials; (d) Tafel curves of various catalysts; (e) LSV curves of NCN-1000-5 with scan rates from 5 to  $100\text{ mV s}^{-1}$ ; (f) the  $i$ - $t$  plot at the applied potential of  $-0.15\text{ V}$  (vs. RHE), inset shows the LSV curves of NCN-1000-5 before and after 500 CV cycles.

Firstly, we investigated the catalytic performance of various active sites for ORR and OER in acidic medium ( $\text{pH}=0$ ) by examining their overpotentials ( $\eta$ ), according to the  $4e^-$  mechanism and computational hydrogen electrode model.<sup>56</sup> More computational details are included in Supporting Information. Figure 9a presents the volcano plot of ORR/OER overpotential versus  $\Delta G(^*O)$  for various active sites on N-doped graphene monolayer, armchair and zigzag graphene nanoribbons. Note that the left/right side of x axis indicates strong/weak interaction between the O atom and the substrates. Obviously, PC has the weakest interaction with O, leading to the poor performance for ORR or OER. Once doped by N atoms, this kind of interaction becomes stronger, thus decreases the overpotential for ORR/OER in some cases. Because the optimal catalytic active site should possess the lowest overpotential, we confirmed that among all the examined possible active sites, the most efficient active site for ORR is the carbon atom, which is at the armchair nanoribbon edge and adjacent to the graphitic N dopant (A-1, Figure 9b). Meanwhile, the most efficient active site for OER is the carbon atom which is near the graphitic N dopant, but  $3.34\text{ \AA}$  away from the armchair ribbon edge (A-3, Figure 9c). We also compared the monolayer models with three different N dopant types (1gN-1, 1pdN-1 and 1prN-1 for the graphitic, pyridinic, and pyrrolic N, respectively). Among these models, 1gN-1 has smallest overpotential, indicating that the graphitic N plays the key role in enhancing the ORR/OER activities for carbon nanosheets. These results are in consistent with previous reports.<sup>57, 58</sup> Then, the HER activity of NCNs in acidic

medium ( $\text{pH}=0$ ) was evaluated by the descriptor  $\Delta G(^*H)$ , the Gibbs free energy of hydrogen adsorption.<sup>59</sup> An ideal HER catalyst has a nearly zero  $\Delta G(^*H)$  value. Interestingly, the best active site for ORR, namely the carbon atoms at the armchair nanoribbon edge adjacent to the graphitic N dopants (A-1), also has the highest HER activity, and its  $\Delta G(^*H)$  value is  $0.07\text{ eV}$  at the hydrogen coverage of  $1.78\%$  (Figure S25 and 9d). Typically, N-doping leads to different local structures, thus affects the electronic properties of carbon nanosheets, and finally alters the adsorption behavior for H and O atoms. The band structure computation (Figure S26) reveals that graphitic N introduces n-type doping, while pyridinic and pyrrolic N introduce p-type doping in the graphene nanosheets/nanoribbons. According to the plots of Figure 9a and Figure S25, it is concluded that p-type doping favors the adsorption of H atoms, and n-type doping favors the adsorption of O atoms, because O is highly electronegative. The above computations show that the carbon atoms close to the graphitic N dopants are the most active sites for ORR, OER and HER reactions, and graphitic N dopants are more vital than the pyridinic and pyrrolic N dopants. These most active sites are at the armchair edges of our computed models, which corresponds to the armchair edge of the large holes found in experiments. These findings echo the experimental results that the sample prepared at high temperature ( $1000\text{ }^\circ\text{C}$ ), which has more percentage of graphitic N and abundant micropores as well as edge defects, has more enhanced catalytic performance than those prepared at low temperature ( $800\text{ }^\circ\text{C}$ ).

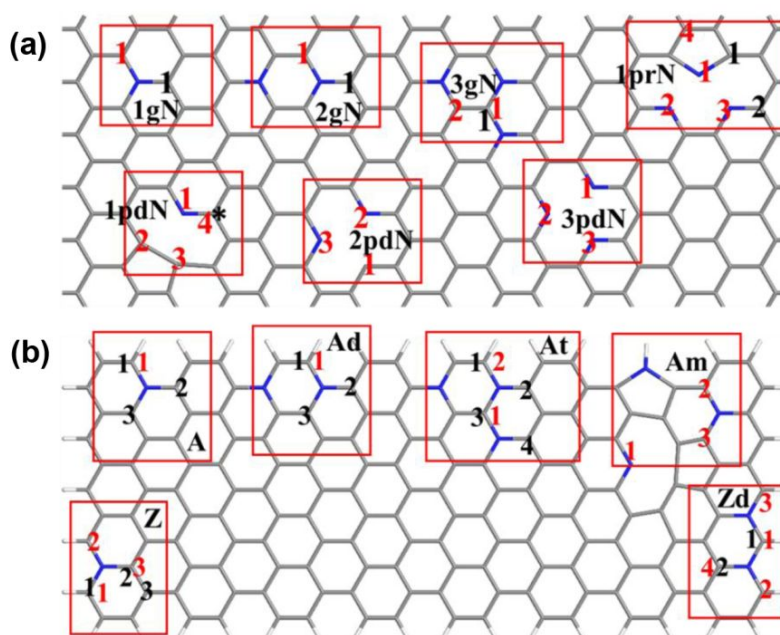


**Figure 8** Schematic presentation of the constructed models. (a) Doped graphene monolayer; (b) doped graphene nanoribbons. The pristine carbon nanosheet is labeled as PC, while the graphitic N, pyridinic N, and pyrrolic N doping modes are marked as ngN, npdN, and nprN separately, where  $n$  ( $1\sim 3$ ) is the number of a specific N dopant in the selected supercell. Labels A, Ad, At, Z, Zd and Am are used for graphene nanoribbons: A and Z denote the armchair and zigzag nanoribbons, d and t mean double and ternary N doping, and m refers to the mixed doping that three N dopants are close to each other. Hereby, the star (\*) and black numbers relate to studied active sites for ORR/OER, whereas the red numbers relate to potential HER active sites. More structural details are in Figure S22 and S23.

### Application in Zn-air battery

As the superior ORR/OER bifunctional electrocatalyst are demanded by metal-air battery,<sup>60</sup> we fabricated a conventional Zn-air battery employing NCN-1000-5 as catalyst in air-cathode (Figure S27). The assembled battery affords a high open circuit voltage of 1.44 V (Figure 10a), close to that of Pt/C+RuO<sub>2</sub> (1.47 V). Figure 10b presents the discharge polarization ( $V$ - $j$ ) curves and the corresponding power density plots. The peak power density of the Zn-air battery equipped with NCN-1000-5

catalyst is calculated to be 207 mW cm<sup>-2</sup>, which is slightly larger than that of Pt/C+RuO<sub>2</sub> (196 mW cm<sup>-2</sup>). As revealed in Figure 10c, the small charge/discharge voltage gap of NCN-1000-5 is approximately equal to that of Pt/C+RuO<sub>2</sub>, indicating their excellent recharge ability when worked as an oxygen electrode bifunctional catalyst in Zn-air batteries. The battery with the NCN-1000-5 air cathode exhibits a voltage platform of 1.21 V (Figure 10d and 10e) at 10 mA cm<sup>-2</sup>, approximating that of Pt/C+RuO<sub>2</sub> (1.25 V). After normalized to the weight of dissipative Zn plate, the high specific capacity and energy

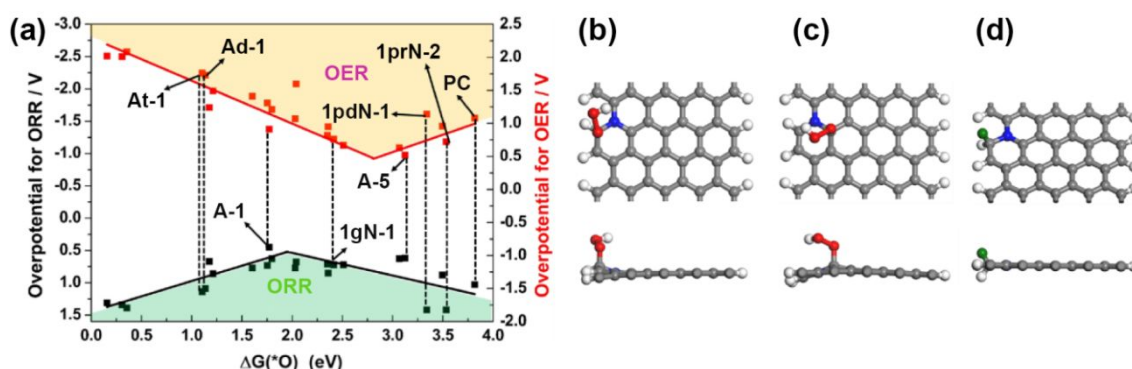


**Figure 9** (a) The volcano plot for ORR and OER by plotting the overpotential as the function of  $\Delta G(^*O)$  at various possible active sites. The top and side views of the active site (b) A-1 for ORR, (c) A-3 for OER with OOH adsorbed, and (d) A-1 for HER, green ball representing the adsorbed H ( $\theta = 1.78\%$ ).

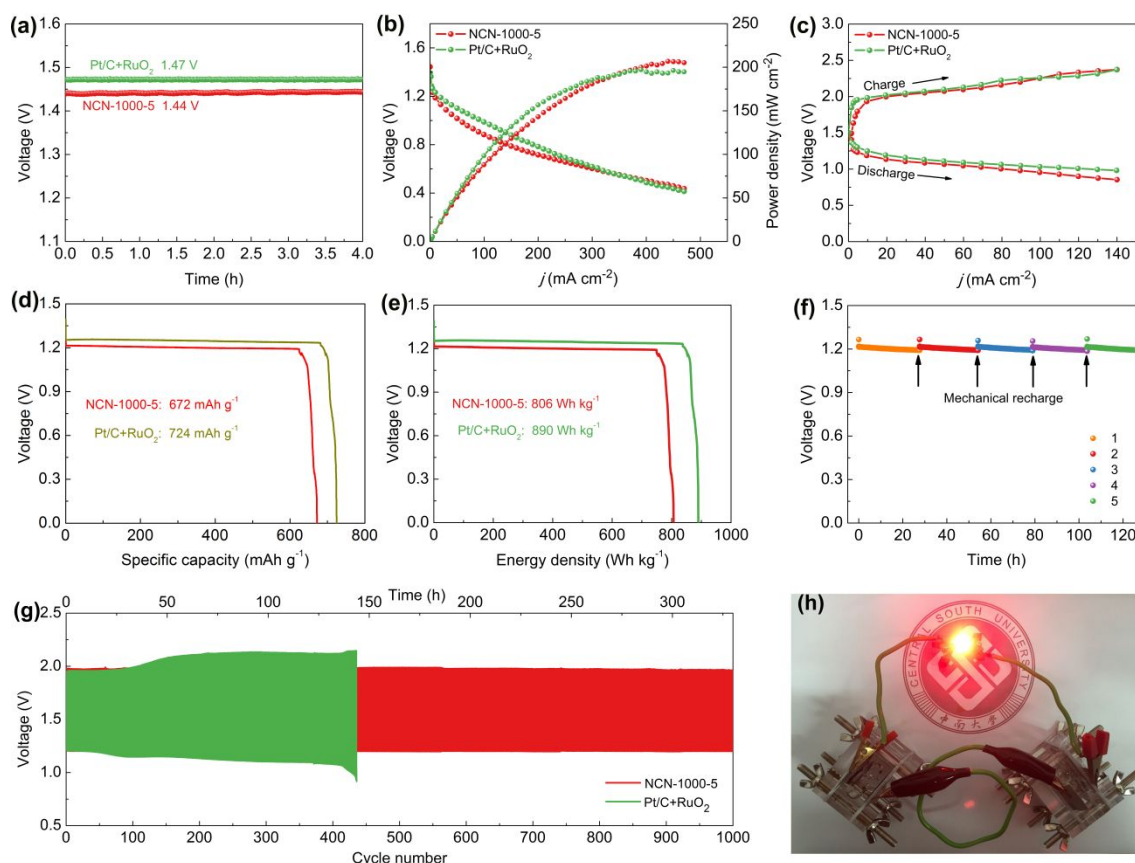


**Figure 10** Zn-air battery performances with NCN-1000-5 acting as the air cathode in comparison with the coupled noble metal Pt/C+RuO<sub>2</sub> catalysts. (a) Open circuit plots, (b) discharge polarization ( $V$ - $j$ ) curves and the corresponding power density curves, (c) charge and discharge polarization ( $V$ - $j$ ) curves, (d) specific capacities and (e) the corresponding energy density plots at 10 mA cm<sup>-2</sup>; (f) long-term stability of the primary Zn-air battery with NCN-1000-5 cathode at 10 mA cm<sup>-2</sup>; (g) galvanostatic discharge and charge cycling curves of the Zn-air battery at 10 mA cm<sup>-2</sup> with 10 min discharge and 10 min charge; (f) photograph of a red LED (2.0 V) powered by two Zn-air batteries based on NCN-1000-5.

density, 672 mAh g<sup>-1</sup> and 805 Wh kg<sup>-1</sup>, are achieved for NCN-1000-5, which are slightly smaller than that of Pt/C+RuO<sub>2</sub> (724 mAh g<sup>-1</sup> and 890 Wh kg<sup>-1</sup>). Gratifyingly, after full discharge, the battery is successfully regenerated by replacing a new Zn plate. Moreover, we do not observe any distinct voltage decline after five cycles at 10 mA cm<sup>-2</sup>, and it maintains continuous discharge over 127 h (Figure 10f), revealing a remarkable long-term durability of NCN-1000-5 for ORR. Furthermore, the cycling performance of the batteries was assessed employing galvanostatic 10 min discharging and 10 min charging at 10 mA cm<sup>-2</sup> (Figure 10g). Initially, the battery equipped with NCN-1000-5 catalyst affords a discharging voltage of 1.21 V and charging voltage of 1.98 V, with a diminutive voltage gap of 0.77 V and a high initial round-trip efficiency of 61.1 %. After 1000 continuous charge/discharge cycles (about 330 h), the voltage gap of NCN-1000-5 air cathode keeps almost unchanged (Figure S28). Whereas, a distinct deterioration is observed for Pt/C+RuO<sub>2</sub> air cathode in a less cycling period (436 cycles, about 145 h), with an enlarged voltage gap of 0.47 V. More importantly, the preeminent discharging capability and cycling performance of Zn-air battery equipped with NCN-1000-5 are also comparable to or even better than those of

reported advanced bifunctional catalysts (Table S14). To demonstrate the feasibility for energy supply in some practical power devices, several Zn-air batteries connected in series were constructed and integrated into circuits. As exemplified in Figure 9h, two concatenated Zn-air batteries equipped with NCN-1000-5 catalyst can provide sufficient voltage to power a red LED (2.0 V). Hence, these results sufficiently illustrate that the NCN-1000-5 can be worked as a promising bifunctional oxygen electrode catalyst for metal-air battery.

## Conclusions

In summary, we have developed a spontaneous gas-foaming strategy to fabricate neoteric nitrogen doped carbon nanosheets (NCN-1000-5) with abundant micropores and edge defects, unique ultrathin nanosheets architecture and ultrahigh specific surface area. These exceptional advantages endow NCN-1000-5 superior trifunctional electrocatalytic activities and strong durability for simultaneous ORR, OER and HER. DFT calculations revealed that the carbon atoms located at the armchair edge and adjacent to the graphitic N dopants act as the most active sites for ORR, OER and HER. The theoretical results well explain why

NCN-1000-5 performs the best among our synthesized samples. Due to the superior ORR/OER activity of NCN-1000-5, the rechargeable Zn-air battery using NCN-1000-5 as cathode catalyst exhibited a high energy density, a low charge/discharge voltage gap, an ultrastrong reversibility and cycling stability. These findings are encouraging researchers to synthesize the catalysts with high specific surface area and rich edge defects as much as possible for ORR, OER and HER. This work not only presents an innovative and universal strategy to prepare advanced carbon materials with ultrahigh specific surface area and abundant edge defects, but also provides useful guidance for designing and developing multifunctional metal-free catalyst for various energy-related electrocatalytic reactions.

## Experimental section

The synthesis of NCNs, instruments and measurements, fabrication and measurements of Zn-air batteries are described in the ESI. †

## Conflicts of interest

There are no conflicts to declare.

## Acknowledgements

This work was supported by the National Nature Science Foundation of China (No. 51474255), the Hunan Provincial Science and Technology Plan Project, China(No.2017TP1001), Project of Innovation-Driven Plan in Central South University (2017CX003), State Key Laboratory of Powder Metallurgy in Central South University, Thousand Youth Talents Plan of China, Hundred Youth Talents Program of Hunan, Shenzhen science and technology innovation project (630) and in USA by NSF-CREST Center for Innovation, Research and Education in Environmental Nanotechnology (CIRE2N, No. HRD-1736093). We thank the Photoemission Endstations (BL10B) in National Synchrotron Radiation Laboratory (NSRL) for help in characterizations.

## References

- J. Zhang, Z. Zhao, Z. Xia and L. Dai, *Nature Nanotech*, 2015, **10**, 444-452.
- B. Rausch, M. D. Symes, G. Chisholm and L. Cronin, *Science*, 2014, **345**, 1326-1330.
- J. G. Lee, J. Hwang, H. J. Hwang, O. S. Jeon, J. Jang, O. Kwon, Y. Lee, B. Han and Y.-G. Shul, *J. Am. Chem. Soc.*, 2016, **138**, 3541-3547.
- C. Duan, D. Hook, Y. Chen, J. Tong and R. O'Hayre, *Energy Environ. Sci*, 2017, **10**, 176-182.
- L. Bu, N. Zhang, S. Guo, X. Zhang, J. Li, J. Yao, T. Wu, G. Lu, J.-Y. Ma and D. Su, *Science*, 2016, **354**, 1410-1414.
- L. C. Seitz, C. F. Dickens, K. Nishio, Y. Hikita, J. Montoya, A. Doyle, C. Kirk, A. Vojvodic, H. Y. Hwang, J. K. Nørskov and T. F. Jaramillo, *Science*, 2016, **353**, 1011-1014.
- H. Wang and H. D. Abruña, *J. Am. Chem. Soc.*, 2017, **139**, 6807-6810.
- K. A. Stoerzinger, O. Diaz-Morales, M. Kolb, R. R. Rao, R. Frydendal, L. Qiao, X. R. Wang, N. B. Halck, J. Rossmeisl, H. A. Hansen, T. Vegge, I. E. L. Stephens, M. T. M. Koper and Y. Shao-Horn, *ACS Energy Letters*, 2017, **2**, 876-881.
- J. Yin, Y. Li, F. Lv, Q. Fan, Y.-Q. Zhao, Q. Zhang, W. Wang, F. Cheng, P. Xi and S. Guo, *ACS Nano*, 2017, **11**, 2275-2283.
- Z. Pei, J. Gu, Y. Wang, Z. Tang, Z. Liu, Y. Huang, Y. Huang, J. Zhao, Z. Chen and C. Zhi, *ACS Nano*, 2017, **11**, 6004-6014.
- X. Liu and L. Dai, *Nature reviews materials*, 2016, **1**, 16064.
- H. Jiang, Y. Wang, J. Hao, Y. Liu, W. Li and J. Li, *Carbon*, 2017, **122**, 64-73.
- S. Chen, J. Duan, M. Jaroniec and S. Z. Qiao, *Adv. Mater.*, 2014, **26**, 2925-2930.
- J. Lai, S. Li, F. Wu, M. Saqib, R. Luque and G. Xu, *Energy Environ. Sci*, 2016, **9**, 1210-1214.
- Q. Liu, Y. Wang, L. Dai and J. Yao, *Adv. Mater.*, 2016, **28**, 3000-3006.
- J. Zhang, L. Qu, G. Shi, J. Liu, J. Chen and L. Dai, *Angew. Chem.*, 2016, **128**, 2270-2274.
- Y. Zhang, X. Fan, J. Jian, D. Yu, Z. Zhang and L. Dai, *Energy Environ. Sci*, 2017, **10**, 2312-2317.
- C. Hu and L. Dai, *Adv. Mater.*, 2017, **29**, 1604942.
- H. Hou, L. Shao, Y. Zhang, G. Zou, J. Chen and X. Ji, *Advanced Science*, 2017, **4**, 1600243.
- W.-J. Jiang, L. Gu, L. Li, Y. Zhang, X. Zhang, L.-J. Zhang, J.-Q. Wang, J.-S. Hu, Z. Wei and L.-J. Wan, *J. Am. Chem. Soc.*, 2016, **138**, 3570-3578.
- H. Jiang, Y. Liu, J. Hao, Y. Wang, W. Li and J. Li, *ACS Sustainable Chem*, 2017, **5**, 5341-5350.
- Z. Liu, Z. Zhao, Y. Wang, S. Dou, D. Yan, D. Liu, Z. Xia and S. Wang, *Adv. Mater.*, 2017, **29**, 1606207.
- Z. Zhang, M. Dou, H. Liu, L. Dai and F. Wang, *Small*, 2016, **12**, 4193-4199.
- Y. Jia, L. Zhang, A. Du, G. Gao, J. Chen, X. Yan, C. L. Brown and X. Yao, *Adv. Mater.*, 2016, **28**, 9532-9538.
- C. Tang and Q. Zhang, *Adv. Mater.*, 2017, **29**, 1604103.
- T. Ji, L. Chen, L. Mu, R. Yuan, M. Knoblauch, F. S. Bao and J. Zhu, *Applied Catalysis B: Environmental*, 2016, **182**, 306-315.
- Y. Pan, Y. Zhao, S. Mu, Y. Wang, C. Jiang, Q. Liu, Q. Fang, M. Xue and S. Qiu, *J. Mater. Chem. A*, 2017, **5**, 9544-9552.
- S. S. Shinde, C.-H. Lee, A. Sami, D.-H. Kim, S.-U. Lee and J.-H. Lee, *ACS nano*, 2016, **11**, 347-357.
- Z. Pei, H. Li, Y. Huang, Q. Xue, Y. Huang, M. Zhu, Z. Wang and C. Zhi, *Energy Environ. Sci*, 2017, **10**, 742-749.
- H. Sun, L. Mei, J. Liang, Z. Zhao, C. Lee, H. Fei, M. Ding, J. Lau, M. Li, C. Wang, X. Xu, G. Hao, B. Papandrea, I. Shakir, B. Dunn, Y. Huang and X. Duan, *Science*, 2017, **356**, 599-604.
- W. He, Y. Wang, C. Jiang and L. Lu, *Chem. Soc. Rev.*, 2016, **45**, 2396-2409.
- H. Jiang, C. Li, H. Shen, Y. Liu, W. Z. Li and J. Li, *Electrochim. Acta*, 2017, **231**, 344-353.
- S. H. Ahn and A. Manthiram, *Small*, 2017, **13**, 1603437.

34. Y. Zheng, Y. Jiao, Y. Zhu, Q. Cai, A. Vasileff, L. H. Li, Y. Han, Y. Chen and S.-Z. Qiao, *J. Am. Chem. Soc.*, 2017, **139**, 3336-3339.
35. D. K. Singh, R. N. Jenjeti, S. Sampath and M. Eswaramoorthy, *J. Mater. Chem. A*, 2017, **5**, 6025-6031.
36. Y. Zheng, Y. Jiao, Y. Zhu, L. H. Li, Y. Han, Y. Chen, M. Jaroniec and S.-Z. Qiao, *J. Am. Chem. Soc.*, 2016, **138**, 16174-16181.
37. Y. Zheng, Y. Jiao, Y. Zhu, L. H. Li, Y. Han, Y. Chen, A. Du, M. Jaroniec and S. Z. Qiao, *Nature Communications*, 2014, **5**, 3783.
38. Y. Jiang, L. Yang, T. Sun, J. Zhao, Z. Lyu, O. Zhuo, X. Wang, Q. Wu, J. Ma and Z. Hu, *ACS Catalysis*, 2015, **5**, 6707-6712.
39. Y. Dafeng, L. Yunxiao, H. Jia, C. Ru, D. Liming and W. Shuangyin, *Adv. Mater.*, 2017, **29**, 1606459.
40. L. Zhang, X. Liang, W. Song and Z. Wu, *PCCP*, 2010, **12**, 12055-12059.
41. X. Wang, W. Chen, L. Zhang, T. Yao, W. Liu, Y. Lin, H. Ju, J. Dong, L. Zheng, W. Yan, X. Zheng, Z. Li, X. Wang, J. Yang, D. He, Y. Wang, Z. Deng, Y. Wu and Y. Li, *J. Am. Chem. Soc.*, 2017, **139**, 9419-9422.
42. Y. Tong, P. Chen, T. Zhou, K. Xu, W. Chu, C. Wu and Y. Xie, *Angew. Chem. Int. Ed.*, 2017, **129**, 7227-7231.
43. D. Hulicova-Jurcakova, M. Kodama, S. Shiraishi, H. Hatori, Z. H. Zhu and G. Q. Lu, *Adv. Funct. Mater.*, 2009, **19**, 1800-1809.
44. K. Sakaushi, A. Lyalin, S. Tominaka, T. Taketsugu and K. Uosaki, *ACS Nano*, 2017, **11**, 1770-1779.
45. N.-T. Suen, S.-F. Hung, Q. Quan, N. Zhang, Y.-J. Xu and H. M. Chen, *Chem. Soc. Rev.*, 2017, **46**, 337-365.
46. J. Park, M. Risch, G. Nam, M. Park, T. J. Shin, S. Park, M. G. Kim, Y. Shao-Horn and J. Cho, *Energy Environ. Sci*, 2017, **10**, 129-136.
47. F. Hu, H. Yang, C. Wang, Y. Zhang, H. Lu and Q. Wang, *Small*, 2017, **13**, 1602507.
48. L. Ye, G. Chai and Z. Wen, *Adv. Funct. Mater.*, 2017, **27**, 1606190.
49. Y. P. Zhu, Y. Jing, A. Vasileff, T. Heine and S. Z. Qiao, *Advanced Energy Materials*, 2017, **7**, 1602928.
50. G.-L. Chai, K. Qiu, M. Qiao, M.-M. Titirici, C. Shang and Z. Guo, *Energy Environ. Sci*, 2017, **10**, 1186-1195.
51. D.-G. Lee, S. H. Kim, S. H. Joo, H.-I. Ji, H. Tavassol, Y. Jeon, S. Choi, M.-H. Lee, C. Kim, S. K. Kwak, G. Kim and H.-K. Song, *Energy Environ. Sci*, 2017, **10**, 523-527.
52. H. Liu, Q. He, H. Jiang, Y. Lin, Y. Zhang, M. Habib, S. Chen and L. Song, *ACS Nano*, 2017, **11**, 11574-11583.
53. Z. Zhao, M. Li, L. Zhang, L. Dai and Z. Xia, *Adv. Mater.*, 2015, **27**, 6834-6840.
54. Z. Zhao and Z. Xia, *ACS Catalysis*, 2016, **6**, 1553-1558.
55. Z. W. Seh, J. Kibsgaard, C. F. Dickens, I. Chorkendorff, J. K. Nørskov and T. F. Jaramillo, *Science*, 2017, **355**.
56. J. K. Nørskov, J. Rossmeisl, A. Logadottir, L. Lindqvist, J. R. Kitchin, T. Bligaard and H. Jónsson, *The Journal of Physical Chemistry B*, 2004, **108**, 17886-17892.
57. M. Li, L. Zhang, Q. Xu, J. Niu and Z. Xia, *J. Catal.*, 2014, **314**, 66-72.
58. Z. Zhao, M. Li, L. Zhang, L. Dai and Z. Xia, *Adv. Mater.*, 2015, **27**, 6834-6840.
59. R. Parsons, *Transactions of the Faraday Society*, 1958, **54**, 1053-1063.
60. I. S. Amiinu, Z. Pu, X. Liu, K. A. Owusu, H. G. R. Monestel, F. O. Boakye, H. Zhang and S. Mu, *Adv. Funct. Mater.*, 2017, **27**, 1702300.